IEEE/ASME Transaction on Mechatronics (Early Access)

# Novel Acoustic Failure Prediction Method for Active Magnetic Bearing Systems

E. Hubmann,
F. Weissofner,
D. Steinert,
T. Nussbaumer,
J. W. Kolar

# Novel Acoustic Failure Prediction Method for Active Magnetic Bearing Systems

Emanuel J. Hubmann, *Graduate Student Member, IEEE*, Fabian Weissofner, Daniel Steinert, Thomas Nussbaumer, and Johann W. Kolar, *Fellow, IEEE*

***Abstract*—For magnetic bearing manufacturers, the installation situations in systems in the field are often unknown and not accessible. Hence, the final system vibration spectrum with respect to excitations by operating the system and therefore mechanical resonances are unknown as well. But to avoid failure, they need to be known before the speed is initially ramped-up in a magnetic bearing suspended system. Therefore, there is a need for an experimental method to predict and prevent already at rotor standstill risks due to plant mechanical resonances. This article shows theoretically and experimentally that conventional magnetic bearing rotor displacement measurement is insensitive on mechanical system resonances. As a solution, two new acoustic response methods are proposed, which can completely detect the system mechanical resonances that will occur during operation already in the standstill levitating state. Furthermore, it is shown with application case studies that these methods can be used for condition monitoring to detect deteriorating changes in the system before rotor speed ramp-up.**

***Index Terms*—Acoustics, active magnetic bearings (AMBs), condition monitoring, damage prediction, self-bearing motors, vibration.**

## I. Introduction

ACTIVE magnetic bearings (AMBs) are installed as components into industrial systems. Their mechanical properties differ, leading to different system vibration (SV-)spectra and, thus, mechanical resonance frequencies of each system. These resonances are excited during operation if they correspond to the rotor speed $\Omega$ or harmonics thereof. This can lead to crash, damage, or even destruction of parts of the system or long-term damage. To help in avoiding such expensive failures in AMB systems, the following prediction methods for AMB systems are needed.

1) Experimental method for quantification of structural optimization attempts regarding dampening or shifting of mechanical resonances before speed ramp-up.
2) Identification prior to speed ramp-up of speed ranges in the operating range $[0, \Omega_{\text{max}}]$, at which mechanical resonances are substantially excited in the system and, therefore, should be avoided for continuous operation (in this article called mechanical resonance speed ranges).
3) Condition monitoring of structural health allowing for health assessment before the system is (re-)started.

This article shows that the state-of-the-art methods are limited and how these limitations can be overcome with novel acoustics-based methods. For all those methods, the SV-spectrum is needed before the speed is ramped-up. It is state of the art to diagnose AMB problems using the AMBs' internal signals such as rotor displacement measurement (RD-M) [1], [2], [3], [4], [5], [6], [7], [8], [9], [10]. An Internet of Things (IoT) application for processing those signals was reported recently in [2]. However, this article shows that RD-M is not suited to gain the SV-spectrum needed. It is impossible with RD-M to detect vibrations that have a node at the AMBs RD-M sensing location, or that do not result in relative radial displacement between the rotor and stator there. The same applies if vibration sensors as in [11] would be used. Although these vibrations are not measurable by RD-M, they emit airborne (i.e., transmitted through air) acoustic emissions, with a new possibility of detecting them.

The use of airborne acoustic emissions for detection and diagnosis during operation of machines in general has been investigated in [12], [13], and [14]. In addition, the monitoring of structure-borne (i.e., transmitted through the structure) noise in rotors with regard to crack formation has been investigated in [15], [16], and [17]. However, this requires physical contact from the piezo-sensor to the spinning rotor body. This has been solved in the literature by wireless communication from the spinning rotor to the stationary evaluation device [15] or via a structure-borne sound conducting mechanical contact via the stationary outer ring of a ball bearing [17]. There, structure-borne noise generated by crack growth or plastic deformation in the range of several 100 kHz is measured by a bonded sensor. Therefore, the occurrence of degradation events in the rotor during operation can be detected, but not the health state as such.

Manuscript received 10 June 2022; revised 31 March 2023 and 19 May 2023; accepted 7 July 2023. Recommended by Technical Editor Y. Liu and Senior Editor R. Gao. This work was supported in part by the Swiss Innovation Agency Innosuisse and in part by Levitronix GmbH. *(Corresponding author: Emanuel J. Hubmann.)*

Emanuel J. Hubmann and Johann W. Kolar are with the Power Electronic Systems Laboratory ETH Zurich, 8092 Zurich, Switzerland (e-mail: hubmann@lem.ee.ethz.ch; kolar@lem.ee.ethz.ch).

Fabian Weissofner, Daniel Steinert, and Thomas Nussbaumer are with the Levitronix GmbH Zurich, 8048 Zurich, Switzerland (e-mail: fabian.weissofner@levitronix.com; steinert@levitronix.com; nussbaumer@levitronix.com).

Color versions of one or more figures in this article are available at https://doi.org/10.1109/TMECH.2023.3301815.

Digital Object Identifier 10.1109/TMECH.2023.3301815

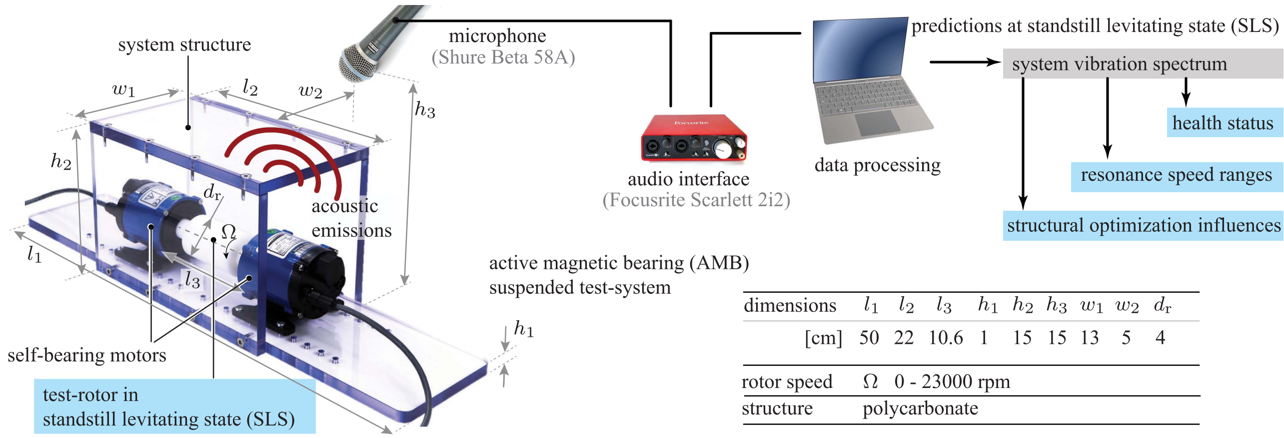


| dimensions | $l_1$ | $l_2$ | $l_3$ | $h_1$ | $h_2$ | $h_3$ | $w_1$ | $w_2$ | $d_r$ |
|---|---|---|---|---|---|---|---|---|---|
| [cm] | 50 | 22 | 10.6 | 1 | 15 | 15 | 13 | 5 | 4 |
| rotor speed | $\Omega$ | 0 - 23000 rpm | | | | | | | |
| structure | polycarbonate | | | | | | | | |

Fig. 1. Proposed novel methods and the 23k r/min double self-bearing motor test system. Acoustic emissions of the AMB system are recorded with a microphone in the SLS. From this, the SV spectrum is obtained. Predictions on health status, mechanical resonance speed ranges, and structural optimization influences can be made.

In [18], a procedure was proposed to monitor cracks in rotors suspended with mechanical bearings and using an AMB as an excitation source only and position sensors to measure the differing rotor response to the excitation in the presence of a rotor crack.

However, to the best of the authors' knowledge, for systems with AMBs, the usage of the information conveyed in the airborne acoustic domain for diagnosis or assessment is not covered in the literature, although the field of AMBs is a very active field of research. Only few efforts touching acoustics in AMB systems for other purposes were reported. In [19], the control signal filtering procedure for reduction of AMB acoustic noise due to electromagnetic interference (EMI) was reported. In [20], the AMB was used to generate antinoise to reduce fluid dynamic-induced noise from an AMB suspended fan. Recently, an advanced control strategy to reduce vibrations (i.e., also acoustic noise) of magnetically suspended rotors was reported in [21]. The monitoring and diagnosis of the application process-related quality in machining was reported in [5] and [22].

In contrast to the field of systems with AMBs, the acoustic emissions were more in focus of research activities for mechanically suspended electric motors. They may be grouped into the three topics: asset diagnosis, emission prediction, and mitigation. Two recent publications addressed the condition monitoring of electric motors with data fusion of acoustic and motor data. In [23], electric faults and faults of rotating parts were diagnosed combined acoustically and with winding current data. In [24], acoustic data were combined with vibration sensor data targeting ball bearing damage. The prediction and mitigation of acoustic emissions of mechanically suspended electric machines gained increasing attention in the recent years with the rise of electric vehicle (EV) technology. To model, predict, and reduce noise, vibration, and harshness (NVH) emissions of electric machine designs, which would be experienced by passengers, simulation frameworks were reported. With modern commercially available software, it is possible to listen to a digital motor-model in operation already during the design phase [25]. This enables design optimizations incorporating the acoustic footprint of electric machines. Example application targets of these activities were EV traction motors [26], [27], [28], [29] or a high-speed air compressor motor for fuel cell EVs [30].

None of these reported works fulfill the three needs stated in the beginning of this section. As a solution, the novel methods presented in this article provide the needed SV-spectrum based on airborne acoustic emissions, already in the standstill levitating state (SLS) before the speed is ramped up. In the following, "airborne" is assumed but no longer explicitly stated. Fig. 1 shows the methods. A double self-bearing motor test-system (SBM)(i.e., AMB and motor function combined in one unit) with rotor speeds of up to 23k r/min from [31] is used along with acoustic recording and processing equipment to demonstrate the novel methods. In the SLS of the rotor, i.e., before speed ramp-up, acoustically the SV-spectrum is measured. It can then be used for experimental structural optimization quantification, identification of mechanical resonance speed ranges, or structural health monitoring.

The rest of this article is organized as follows. In Section II, the capability of RD-M to measure the SV-spectrum is investigated with the aid of a mathematical system model. The RD-M is shown to fail to measure the SV-spectrum in the model. Two acoustic disturbance force excitation response (DF-ER) measurement methods are introduced in Section III. They serve as a basis for the acoustic prediction of mechanical resonances in SLS. These methods are validated with 3D finite element method (3D-FEM) modal analysis and a speed ramp-up experiment in Section IV. It is shown experimentally that the AMB RD-M fails to measure the SV-spectrum. Three case studies for the application of the novel methods are presented in Section V. Finally, Section VI concludes this article.

## II. Mechanical Resonance Measurement: AMB-Limitations and Acoustic Advantages

In their ability to measure mechanical vibrations, RD-M and acoustic emission measurement (AE-M) differ in two basic prin-

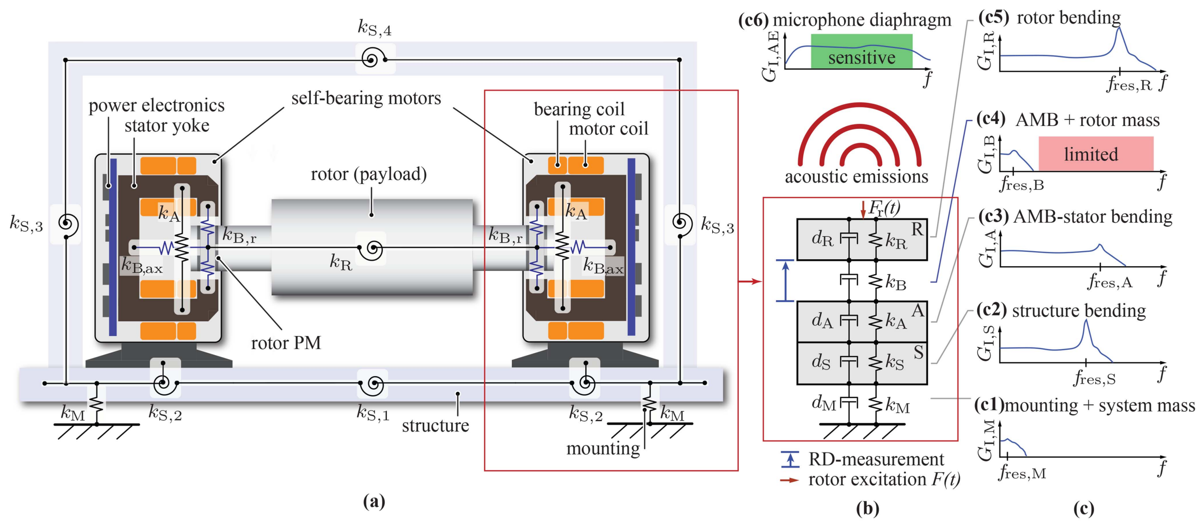


Fig. 2. (a) Simplified conceptual model of the test-system with stiffnesses $k_i$: rotor bending stiffness $k_{\mathrm{R}}$, AMB stiffness $k_{\mathrm{B}}$, AMB-stator bending stiffnesses $k_{\mathrm{A}}$, system structure stiffnesses $k_{\mathrm{S}}$, and mounting stiffness $k_{\mathrm{M}}$. (b) Further simplified model in abstracted form. (c) Typical individual disturbance force excitation response $G_{\mathrm{I},i}$ to force excitation on the corresponding mass $m_i$ of the subcomponents.

ciples. First, RD-M measures only locally, whereas AE-M can sense emissions from vibrations throughout the entire system. Thus, RD-M cannot measure vibration modes with vibration nodes at the RD-M locations, whereas AE-M can, because of its global nature. Second, the physical quantity being measured is different. The RD-M measures a physical distance between two objects, AE-M measures sound waves. Vibrating parts emit sound waves, i.e., they can be measured by AE-M. Further, it is unclear how the RD-M is related to system vibrations. This is investigated in the following by breaking the system down into mass–spring–damper (mkd-)element subcomponents and discussion of their individual DF-ER in Section II-A, and by mathematically modeling the combined system and investigating its combined DF-ER to rotor forces in Section II-B.

## A. System Model $mkd$-Subcomponents

Fig. 2(a) shows a simplified model of the test-system depicted in Fig. 1. Subcomponents exhibiting vibration modes are represented lumped as spring symbols $k_i$. Each of these subcomponents possesses an attributed mass and damping. This results in (mkd-)elements, which are described in the following: as commonly done [32], an AMB with proportional-derivative position control (cf., [33]) can be modeled as a spring–damper ($k_{\mathrm{B}}$, $d_{\mathrm{B}}$) element if linearized at the operating point. In the test-system, the rotor position is radially actively controlled, whereas axially it is passively stabilized by reluctance forces. The AMB stiffness in Fig. 2(a) is, thus, further distinguished into the radial stiffness $k_{\mathrm{B,r}}$ and the axial $k_{\mathrm{B,ax}}$ one. The stiffnesses for bending modes are generalized indicated as rotor $k_{\mathrm{R}}$, self-bearing motor stator $k_{\mathrm{A}}$, and structural $k_{\mathrm{S},i}$ bending stiffnesses. The mounting support stiffness is labeled as $k_{\mathrm{M}}$.

For simplicity and generalization, in Fig. 2(b), the complexity of the system model is further reduced. In Fig. 2(c), the individual DF-ERs $G_{\mathrm{I,i}}$ from the disturbance force excitation $F_i$ on the corresponding mass $m_i$ to the deflection $x_i$ of the subelements from Fig. 2(b) are qualitatively shown.

All modeled subelements behave individually as mkd-elements. They represent a second-order system. Newton's second law yields

$$m_i \ddot{x}_i = -k_i x_i - d_i \dot{x}_i + F_i(t). \tag{1}$$

resulting in the subcomponent transfer function $H_i(s)$ from DF-E $F_i(t)$ on the mass $m_i$ to the position $x_i$

$$H_i(s) = \frac{X_i(s)}{F_i(s)} = \frac{1}{m_i s^2 + d_i s + k_i} \tag{2}$$

which for no damping $d_i$ leads to a resonance frequency $f_{\mathrm{res},i}$ of

$$f_{\mathrm{res},i} = \frac{1}{2\pi} \cdot \sqrt{\frac{k_i}{m_i}}. \tag{3}$$

Above $f_{\mathrm{res},i}$, the mkd-elements show a low-pass filter (LPF) characteristic. The coupling of the test-system to ground in Fig. 2(c1) is done in a soft way. It was placed on a foam mat resulting in an $f_{\mathrm{res,M}}$ in the range of 60 Hz. The structural resonances in Fig. 2(c2) show higher $f_{\mathrm{res,S}}$. The same holds for AMB stator bending $f_{\mathrm{res,A}}$ in Fig. 2(c3). In contrast to that, the combination of rotor mass and AMB stiffness in Fig. 2(c4) leads to a very low $f_{\mathrm{res,B}}$, in the test-system in the range of 24 Hz (axial), 45 Hz (cylindrical) 70–100 Hz (conical modes) [31]. Rotor bending modes of the test-system in Fig. 2(c5) show $f_{\mathrm{res,R}}$ above 1.5 kHz [31]. The sensitivity of a microphone diaphragm in Fig. 2(c6) remains high over a large frequency range due to its low inertia. The microphone used in this article, Shure Beta 58 A, has a high sensitivity in the range of 50 Hz–16 kHz [34].

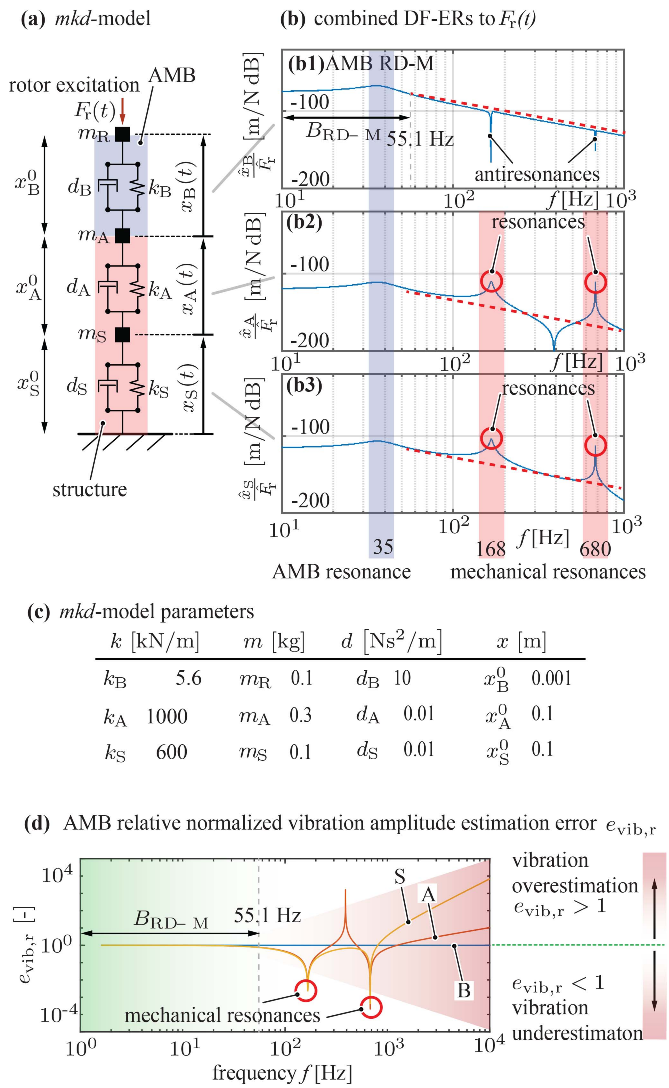


Fig. 3. (a) mkd-model used for the mathematical analysis. (b) Combined disturbance force excitation responses (DF-ERs) from rotor force excitation $F_r(t)$ to the corresponding deflections $x_i$. (c) mkd-model parameters of the analysis. (d) AMB relative normalized vibration amplitude estimation error.

## B. Combined DF-ERs and AMB Relative Normalized Vibration Amplitude Estimation Error

To investigate the combined DF-ERs to rotor forces, the mkd-model in Fig. 2(b) is further simplified by omitting the low-frequency mounting support $k_M$, resulting in the mkd-model in Fig. 3(a). In the following, a state space system representation of the mkd-model is derived in the form

$$\underline{\dot{x}} = \underline{A} \cdot \underline{x} + \underline{B} \cdot \underline{u} \tag{4}$$

$$\underline{y} = \underline{C} \cdot \underline{x}\,. \tag{5}$$

The individual distances $x_i$ between the masses $m_i$, and their time derivatives serve as the system states $\underline{x}$. As inputs $\underline{u}$ serve the constant neutral (zero force) distances $x_i^0$ of the springs $k_i$ and the time varying rotor excitation force $F_r(t)$

$$\begin{bmatrix} \dot{x}_A \\ \dot{x}_B \\ \dot{x}_C \end{bmatrix} := \begin{bmatrix} x_4 \\ x_5 \\ x_6 \end{bmatrix},\ \underline{x} = \begin{bmatrix} x_A \\ x_B \\ x_C \\ x_4 \\ x_5 \\ x_6 \end{bmatrix},\ \underline{u} = \begin{bmatrix} x_A^0 \\ x_B^0 \\ x_C^0 \\ F_r(t) \\ 0 \\ 0 \end{bmatrix}. \tag{6}$$

with $\Delta_i$ being the deflection of the corresponding mkd-element

$$\Delta_i = x_i - x_i^0\,. \tag{7}$$

Newton's second law yields

$$m_S \cdot \ddot{x}_S = -\Delta_S k_S - \dot{x}_S d_S + \Delta_A k_A + \dot{x}_A d_A \tag{8}$$

$$m_A \cdot (\ddot{x}_S + \ddot{x}_A) = -\Delta_A k_A - \dot{x}_A d_A + \Delta_B k_B + \dot{x}_B d_B \tag{9}$$

$$m_B \cdot (\ddot{x}_S + \ddot{x}_A + \ddot{x}_B) = -\Delta_B k_B - \dot{x}_B d_B + F_r(t)\,. \tag{10}$$

Accordingly the system matrices of the state space representation can be derived to

$$\underline{A} = \begin{bmatrix} 0 & 0 & 0 & 1 & 0 & 0 \\ 0 & 0 & 0 & 0 & 1 & 0 \\ 0 & 0 & 0 & 0 & 0 & 1 \\ -\frac{k_S}{m_S} & \frac{k_A}{m_S} & 0 & -\frac{d_S}{m_S} & \frac{d_A}{m_S} & 0 \\ \frac{k_S}{m_S} & -\frac{k_A}{m_S} - \frac{k_A}{m_A} & \frac{k_B}{m_A} & \frac{d_S}{m_S} & -\frac{d_A}{m_S} - \frac{d_A}{m_A} & \frac{d_B}{m_A} \\ 0 & \frac{k_A}{m_A} & -\frac{k_B}{m_A} - \frac{k_B}{m_B} & 0 & \frac{d_A}{m_A} & -\frac{d_B}{m_A} - \frac{d_B}{m_B} \end{bmatrix} \tag{11}$$

$$\underline{B} = \begin{bmatrix} 0 & 0 & 0 & 0 & 0 & 0 \\ 0 & 0 & 0 & 0 & 0 & 0 \\ 0 & 0 & 0 & 0 & 0 & 0 \\ \frac{k_S}{m_S} & -\frac{k_A}{m_S} & 0 & 0 & 0 & 0 \\ -\frac{k_S}{m_S} & \frac{k_A}{m_S} + \frac{k_A}{m_A} & -\frac{k_B}{m_A} & 0 & 0 & 0 \\ 0 & -\frac{k_A}{m_A} & \frac{k_B}{m_A} + \frac{k_B}{m_B} & \frac{1}{m_B} & 0 & 0 \end{bmatrix} \tag{12}$$

where $\underline{C}$ is an identity matrix, returning the states $\underline{x}$ in the output $\underline{y}$. With this state space representation, the DF-ERs were computed for all three mkd-elements w.r.t. the rotor excitation, presented in Fig. 3(b). Thereby, the model parameters shown in Fig. 3(c) were used. The bearing stiffness $k_B$ corresponds to the measured value of the test-system from [31]. Compared with its low $k_B$ and high $d_B$, high structural stiffness ($k_A, k_S$) and low structural damping ($d_A, d_S$) were analyzed to represent structural behavior. The AMB RD-M shows for low frequencies a damped resonance and for higher frequencies a LPF characteristic and two antiresonances in Fig. 3(b1). In the presence of RD-M sensor noise, those antiresonances are partially covered by the noise. In contrast to the RD-M, both structure-related mkd-systems show two distinct resonances in Fig. 3(b2) and (b3). Therefore, the rotor excitation force $F_r(t)$ at those frequencies excites mechanical resonances, whereas the AMB mkd-system is not excited, it even shows antiresonances. To quantify how well the AMB RD-M can measure the mechanical

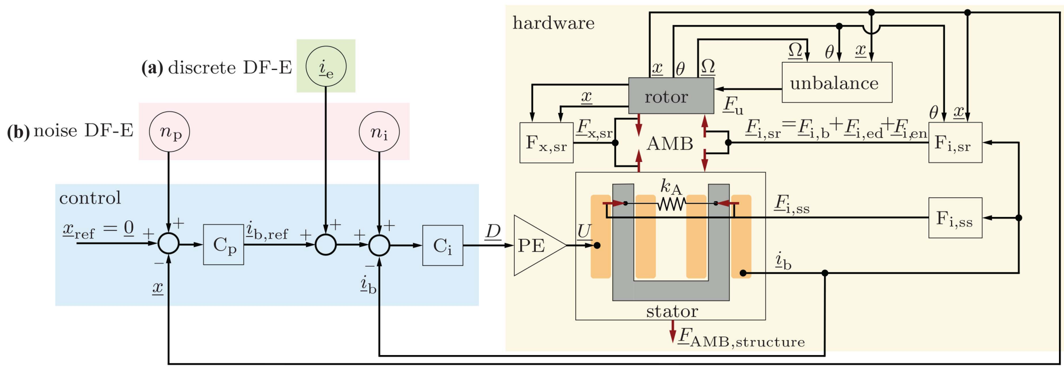


Fig. 4. Two proposed excitation methods are (a) active superimposed discrete disturbance force excitation (discrete DF-E) as $\underline{i}_{\mathrm{e}}$ on the reference current at the output of the position controller $\mathrm{C_p}$ and (b) noise disturbance force excitation (noise DF-E) as the coupling of noise sources by, e.g., noise $n_{\mathrm{p}}$ on the position signal or noise $n_{\mathrm{i}}$ on the current measurement. Resulting excitation forces between stator and rotor $\underline{F}_{\mathrm{i,ed}}$ and $\underline{F}_{\mathrm{i,en}}$ are superimposed on the nominal magnetic bearing force $\underline{F}_{\mathrm{i,b}}$ actively generated by the reference bearing current $\underline{i}_{\mathrm{b,ref}}$. Further during rotation, unbalanced forces $\underline{F}_{\mathrm{u}}$ excite the rotor and passive magnetic reluctance forces $\underline{F}_{\mathrm{x,sr}}$ excite both rotor and stator. In addition, excitation forces are generated internally to the stator $\underline{F}_{\mathrm{i,ss}}$.

resonances, the AMB relative normalized vibration amplitude estimation error $e_{\mathrm{vib,r,n}}$ is introduced as

$$e_{\mathrm{vib,r,n}}(f) = \frac{\hat{x}_{\mathrm{B}}(f)}{\hat{x}_{\mathrm{i}}(f)} \cdot \frac{\hat{x}_{\mathrm{i}}(f=0)}{\hat{x}_{\mathrm{B}}(f=0)} \,. \tag{13}$$

If the DF-ER of the AMB RD-M captures the vibrations, then it is proportional to the DF-ERs of the vibrations, i.e., showing the same response characteristic. In that case, $e_{\mathrm{vib,r,n}} = 1$. If the AMB RD-M underestimates vibrations, then $e_{\mathrm{vib,r,n}} < 1$, if it overestimates, $e_{\mathrm{vib,r,n}} > 1$. Fig. 3(d) shows $e_{\mathrm{vib,r,n}}$ for the two structural mkd-subcomponents. For frequencies lower than the RD-M DF-ER bandwidth $B_{\text{RD-M}}$, $e_{\mathrm{vib,r,n}}$ is very close to 1. It should be noted that $B_{\text{RP-M}}$ is defined by the mkd-property of the AMB together with the rotor mass, i.e., no matter how high the bandwidth of an actual position sensor is, the physical quantity measured defines already the upper limit $B_{\text{RD-M}}$. Above $B_{\text{RD-M}}$, $e_{\mathrm{vib,r,n}}$ increasingly deviates from 1, even with sign changes. The mechanical resonances are underestimated by order of magnitudes. The AMB RD-M therefore fails to measure the vibrations present in the system model. This is in alignment with experiences in other fields: in a system with many resonance frequencies, the energy concentrates in the vibration modes with excitation matching the resonance frequency. This is exploited in tuned resonators for the damping of unwanted resonances as reported in [35], [36], and [37]. It is applied, for example, in bridges, skyscrapers, or stringed musical instruments (e.g., "wolftone" eliminator on a cello). Therefore, AMB RD-M shows substantial deficiencies in measuring vibrations, whereas AE-M shows promising characteristics. This is investigated in the following sections.

## III. Acoustic DF-ER Measurement Methods—Basis for Acoustic Prediction of Mechanical Resonances and Validation Thereof

The active nature of AMBs enables us to measure system DF-ERs by exciting and measuring a response, shown for example in [39]. For this purpose, in the SLS, a disturbance force excitation (DF-E) is realized by superimposing a corresponding excitation current $\underline{i}_{\mathrm{e}}$ component on the reference bearing current $\underline{i}_{\mathrm{b,ref}}$. In [7] and [40], instead of or in addition to, the excitation with one discrete frequency $f_{\mathrm{k}}$, a noise component was superimposed on $\underline{i}_{\mathrm{b,ref}}$. In [41], separate excitation winding turns were wound onto the AMB stator.

Fig. 4 shows the two approaches for using the AMB itself as an excitation source: in Fig. 4(a), the excitation current $\underline{i}_{\mathrm{ed}}$ with a discrete frequency and in Fig. 4(b), the excitation with noise $n$. Both are resumed in this article, but in a new form. Instead of the RD-M response, the AE-M system response is measured for both methods. Further, instead of superimposing artificial noise, the naturally present noise in the bearing current is used. Ultimately, the bearing current superpositions lead to additional forces $\underline{F}_{\mathrm{i,ed}}$ and $\underline{F}_{\mathrm{i,en}}$ between rotor and stator. They act like the reference bearing current $\underline{i}_{\mathrm{b,ref}}$ generated nominal bearing force itself $\underline{F}_{\mathrm{i,b}}$ or like unbalance excitations $\underline{F}_{\mathrm{u}}$ or passive magnetic forces $\underline{F}_{\mathrm{x,sr}}$. Since these magnetic forces also act on the stator, they excite the structure with a force $\underline{F}_{\mathrm{AMB,structure}}$. In [10], $\underline{F}_{\mathrm{AMB,structure}}$ was measured and modeled for a Lorentz-type AMB, where (in contrast to the AMBs of the test-system in this article), the passive reluctance force relationships $\mathrm{F_{x,sr}}$ in Fig. 4 played a minor role compared with the current-dependent ones $\mathrm{F_{i,sr}}$. AMB-stator internal forces $\underline{F}_{\mathrm{i,ss}}$ are parasitically generated in the same way and are a possible additional contributor to the system structure excitation.

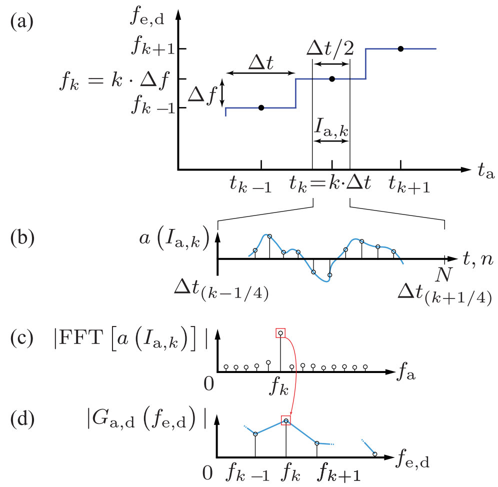


Fig. 5. (a) Realization of discrete DF-E, (b) extraction of half hold-period sized evaluation interval $I_{\mathrm{a},k}$ for each hold period $\Delta t$, (c) discrete fast Fourier transform (FFT) of the evaluation interval data, (d) interpretation of the extracted FFT amplitude of the respective discrete excitation frequency $f_k$ as the $k$th acoustic discrete DF-ER $|G_{\mathrm{a,d}}|$.

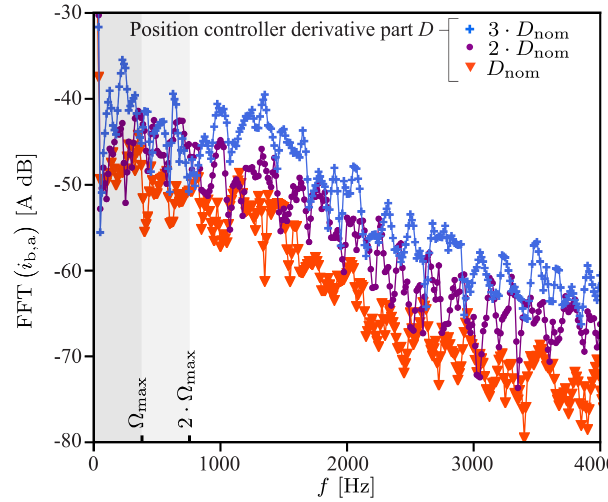


Fig. 6. Example measurement of the bearing current noise spectrum of one bearing phase by FFT transformation of the current measured on the oscilloscope. The bearing current noise spectrum is shown for nominal, doubled, and tripled position controller $D$-part. The noise spectrum is relatively flat in the operating range of the AMB and its magnitude increases with increasing position controller $D$-part.

In the following section, the two types of DF-E methods and corresponding acoustic response measurements are explained in detail.

### A. Acoustic Discrete DF-ER in SLS

A discrete DF-E with one frequency, which is then varied over a frequency range, was realized as a spatially rotating disturbance force vector $\underline{F}_{\mathrm{i,ed}}$. This was implemented by superimposing a sine component corresponding to the excitation frequency in the $x$-direction and a cosine component in the $y$-direction.

Fig. 5 shows the measurement and evaluation procedure. The discrete DF-E was realized as a staircase-shaped discrete frequency sweep presented in Fig. 5(a). For each hold period $\Delta t$, a half hold-period sized evaluation interval $I_{\mathrm{a},k}$ of the acoustic signal was extracted from the permanently running acoustic recording, as presented in Fig. 5(b). The evaluation interval $I_{\mathrm{a},k}$ was subsequently subjected to the discrete fast Fourier transform (FFT) in Fig. 5(c). The amplitude of the respective discrete excitation frequency $f_k$ was extracted and interpreted as the $k$th acoustic discrete DF-ER $|G_{\mathrm{a,d}}|$, as displayed in Fig. 5(d).

### B. Acoustic Natural Bearing Current Noise DF-ER in SLS

The natural noise on the bearing current, which is present in normal operation, i.e., not generated artificially, leads to a DF-E, albeit of very small amplitude. Unavoidable sources of current noise $n_{\mathrm{i}}$ and position measurements noise $n_{\mathrm{p}}$ could be of thermal, $1/f$ decaying (with frequency $f$) [42], and EMI [19] nature. An exemplary measured bearing current frequency spectrum is shown in Fig. 6. The noise spectrum is relatively flat in the operating range up to the maximum speed $\Omega_{\max}$. This low-frequency noise cannot be filtered without impairing the position control. To prove the influence of the position measurement noise, the derivative part ($D$-part) of the PID position controller was doubled and tripled from the nominal value, and the corresponding frequency spectrum was measured. The noise amplitude increases with a higher $D$-part, thus confirming the suspected correlations. This also means that within control stability limits, the $D$-part could be used to artificially increase the noise level. With the nominal $D$-part, the resulting acoustic noise was barely audible; nevertheless, this nominal value was kept constant for all following investigations. To measure the acoustic response to the natural bearing current noise, a short audio sequence was recorded with the rotor in SLS. The FFT of this recording sequence directly yields the acoustic noise DF-ER.

## IV. Validation of Acoustic Mechanical Resonance Prediction in SLS and Failure of AMB RD-M to Achieve the Same

Both acoustic DF-ER measurement methods in SLS presented in Section III were applied to predict the mechanical resonances of the test-system, shown in Fig. 7(a) and (b). This prediction was successfully validated first with 3D-FEM modal analysis of the test system in Fig. 7(a) and second with a speed ramp-up of the test system in Fig. 7(c). As proposed by the derived theory in Section II, the DF-ER of the RD-M at SLS, shown in Fig. 7(d), failed to predict the mechanical resonances, supporting the theory. In the speed ramp-up experiment, the RD-M did not show signs of mechanical resonance detection capability in Fig. 7(e), i.e., the detection failed. This is in accordance with the presented theory in Section II. In summary, the acoustic mechanical resonance prediction in SLS was validated with

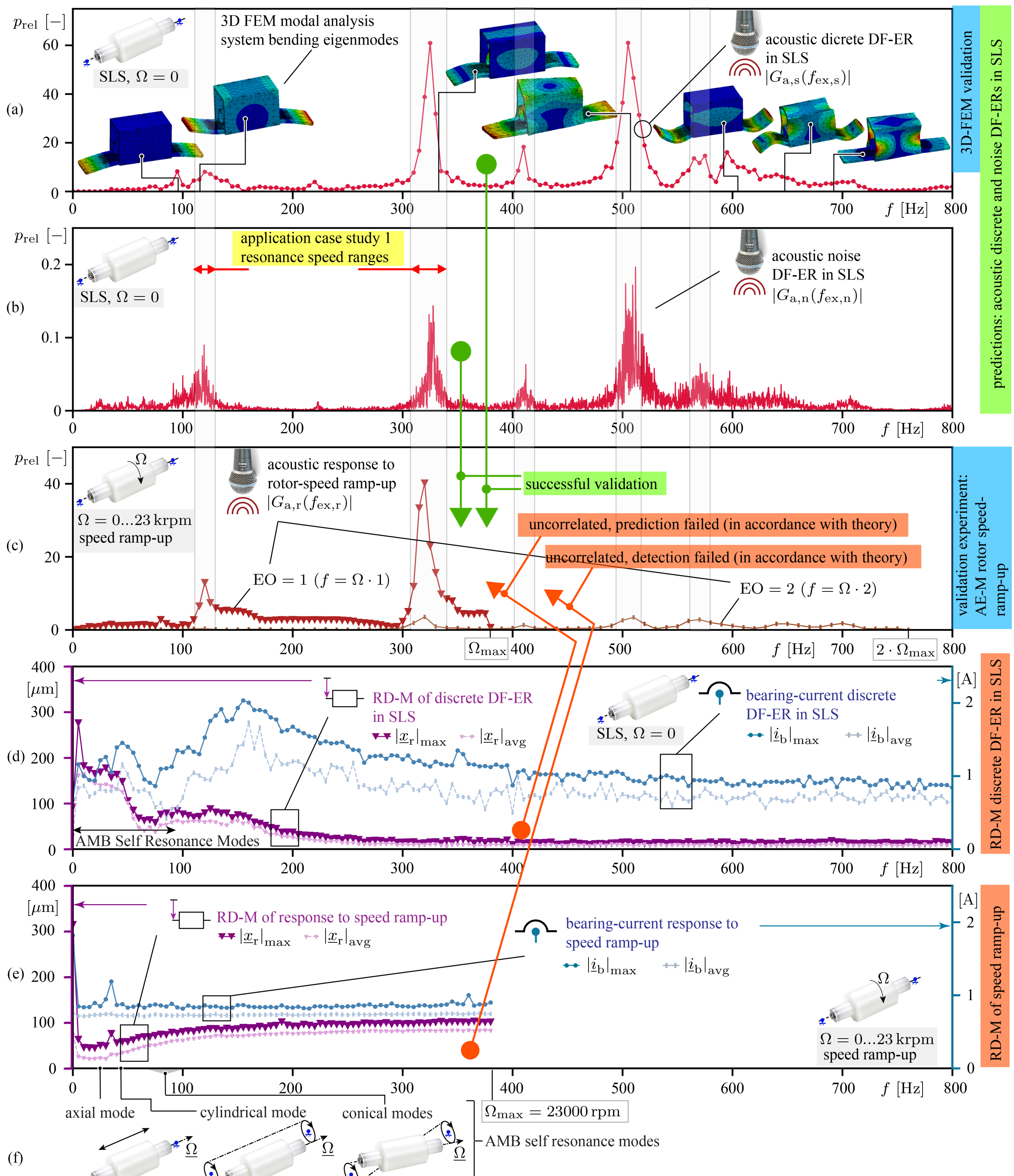


Fig. 7. (a) Successful prediction of mechanical resonances with acoustic discrete DF-ER in SLS and 3D-FEM validation of the acoustic SV-spectrum predictions. (b) Successful prediction of mechanical resonances with acoustic noise DF-ER in SLS and application case study one: identification of mechanical resonance speed ranges. (c) Validation experiment: acoustic response to rotor speed ramp-up, validation of AE-M predictions. (d) Failed RD-M prediction of the SV-spectrum in accordance with the theory. (e) Failed RD-M detection of mechanical resonances during rotor speed ramp-up in accordance with the theory. (f) Indicated AMB self-resonance modes.

simulation and experiment. Furthermore, the theory in Section II was found to be supported by the failure of AMB RD-M to predict in SLS and to detect during operation the mechanical resonances. In the following, the details of the measurements are discussed.

For the validation of the proposed theory and methods, the frequency range was defined to cover frequencies up to twice the rotational frequency (excitation order EO $= 2$) at a maximum test-system speed of $\Omega_{\max} = 23$ k r/min (383 rev/s), i.e., 0–800 Hz. This was done to cover the range, where the main excitations occur during rotating operation, as for higher EOs the excitation magnitude drops. In electric machines, due to the nonideal field shapes, higher harmonics also occur in the magnetic forces and lead to higher order excitations, as shown in, e.g., [26]. For the acoustic measurements, the sound pressure levels provided are normalized pressures $p_{\mathrm{rel}}$, which by normalization with $p_0 = 20\,\mu$Pa, (calibrated at 400 Hz with testo 816-1 sound pressure level measurement unit, testo SE & Co. KGaA, Lenzkirch, Germany). For the discrete DF-E, an amplitude of 400 mA was superimposed on the reference bearing current $\underline{i}_{\mathrm{b,ref}}$.

The prediction of mechanical resonances with acoustic discrete DF-ER in SLS in Fig. 7(a) shows distinct peaks. They are validated twice as mechanical resonances, once with mechanical eigenmodes obtained by 3D FEM modal analysis in Fig. 7(a), and another with the speed ramp-up in Fig. 7(c).

The acoustic noise DF-ER in Fig. 7(b) and the discrete one in Fig. 7(a) show the same SV-spectrum profile with very good agreement. The noise DF-ER signal is two orders of magnitude weaker, but does not show less information content, i.e., similar information from discrete DF-ER can be obtained by noise DF-ER. It further confirms the cause–effect chain in Fig. 4. This similarity means that the same double validation as for the discrete DF-ER applies similarly for this noise-based method.

The validation experiment in Fig. 7(c) is a speed ramp-up from 0 to 23 k r/min. The same procedure as for the discrete DF-ER was used for evaluation, but instead of artificial excitation, the natural excitations due to speed ramp-up operation were present. Simultaneously, both EO $= 1$ and EO $= 2$ were evaluated for each rotational speed $\Omega$. Deviations in magnitude compared with the discrete and noise DF-ER were expected due to the different nature of excitation. Vibration modes with natural frequencies higher than the maximum rotational frequency of the rotor are excited by the excitations with EO $= 2$ during the run-up, and these peaks also agree with the acoustic predictions in SLS [see Fig. 7(a) and (b)].

The acoustic predictions in SLS and speed ramp-up validation experiment are further compared with the AMB internal discrete DF-ER in SLS shown in Fig. 7(d). Neither the maximum or average rotor displacement ($|\underline{x}|_{\max}$ and $|\underline{x}|_{\mathrm{avg}}$) nor the measured bearing currents (maximum and average magnitude of bearing current space vector $|\underline{i}_{\mathrm{b}}|_{\max}$ and $|\underline{i}_{\mathrm{b}}|_{\mathrm{avg}}$) show distinct resonance peaks corresponding to the validation experiment in Fig. 7(c). Only in the region of the AMB-rotor mkd-self-resonances in Fig. 7(f), large peaks in the measured rotor position $|\underline{x}_{\mathrm{r}}|$ are found. Slightly above these resonances, the LPF characteristic of the AMB becomes apparent with decreasing rotor displacements in accordance with the theory in Section II.

Also during speed ramp-up no signs of mechanical resonance-induced peaks were found in the AMB internal RD-M and bearing currents shown in Fig. 7(e). Above its resonance frequency, the AMB becomes self-centering. Geometric rotor asymmetries are still perceived ($< 50\,\mu$m for this test-system) due to the high position sensor bandwidth. Force rejection methods, as summarized in [3] and [38], allow the position sensors to ignore those supposed oscillations and let the rotor rotate around its principal axis of inertia, explaining the asymptotically reached rotor deflection offset. In accordance with the theory in Section II, the AMB failed to detect the mechanical resonances occurring during operation.

Summarizing, the theoretical considerations in Section II are confirmed experimentally. Both acoustic methods that were introduced to predict mechanical resonances in SLS were successfully validated with 3D-FEM modal analysis and experimentally, whereas as expected the AMB RD-M failed to achieve that prediction.

## V. Acoustic Failure Prediction at Standstill

In Section IV, it was shown that both proposed acoustic DF-ER methods can provide a SV-spectrum. A healthy system possesses a certain characteristic SV-spectrum. It can, therefore, serve as a reference, against which condition monitoring can be done. Faults that result in a change in the SV-spectrum due to, e.g., change in stiffnesses, damping, mass distributions, or excitation transmission change can therefore be detected. In the following, this capability is exemplary demonstrated with three application case studies. By means of the two acoustic methods presented in this article, it is possible to detect such a system fault acoustically even in SLS before the speed is ramped up, i.e., predict a potential system failure before it can occur.

### A. Application Case Study 1: Mechanical Resonance Speed Ranges

Both noise and discrete DF-ER prediction of the SV-spectrum are used to identify mechanical resonance speed ranges. These speed ranges should be excluded from continuous operation due to excessive mechanical vibrations. They are shown in Fig. 7(b). It should be noted, however, that resonance frequencies that do not originate from the stationary structure but from the rotor can deviate from the value identified at SLS with increasing speed due to gyroscopic effects.

### B. Application Case Study 2: Lost AMB Mounting Screws

Three out of four fastening screws of one AMB were removed, which represents a severe fault with system failure potential. The fault resulted in a change in the SV-spectrum. The acoustic discrete DF-ER in SLS is shown in Fig. 8(a) in healthy, and in Fig. 8(b), in damaged condition. Fig. 8(c) shows the acoustic

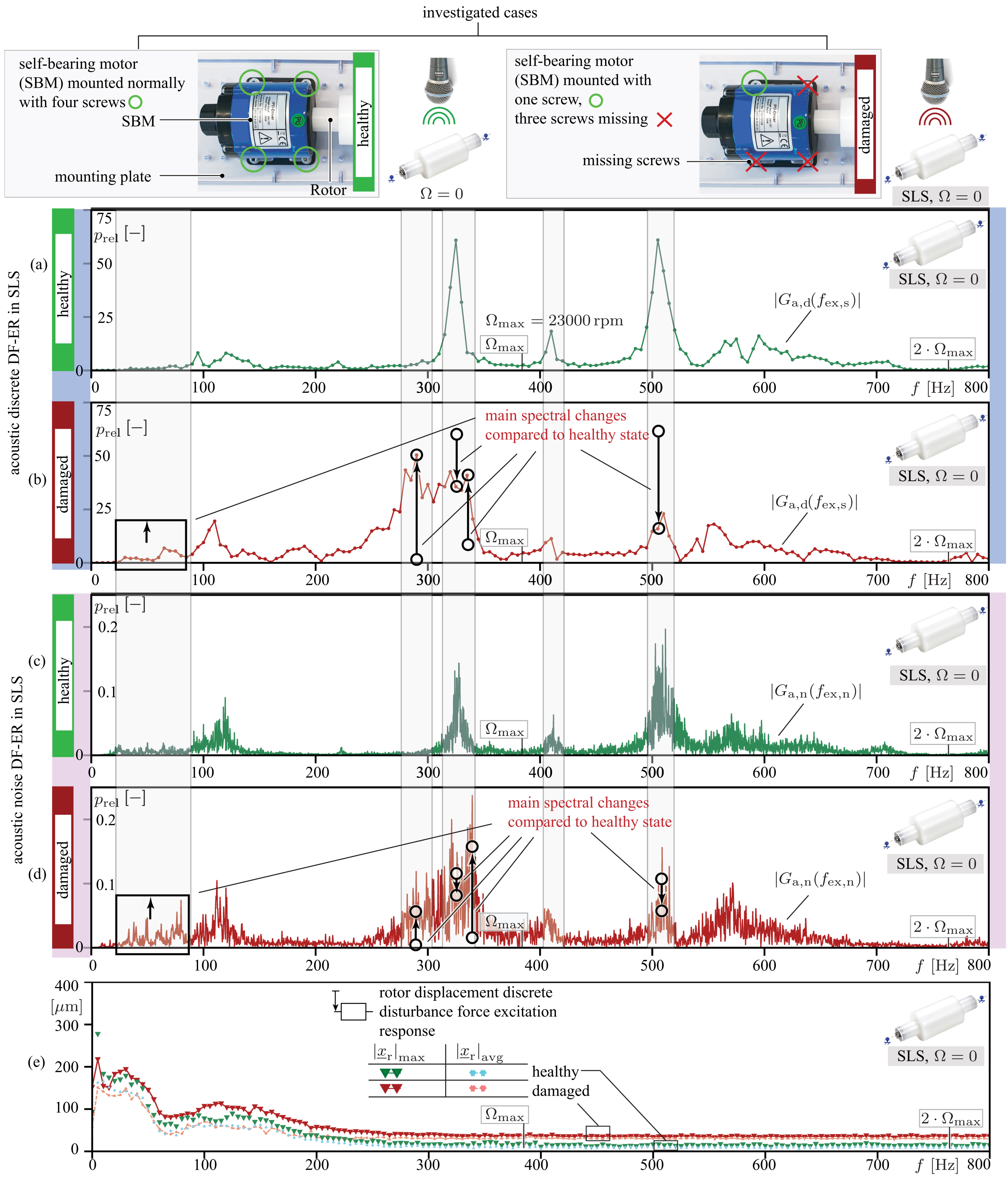


Fig. 8. Acoustic failure risk prediction: comparison of the acoustic DF-ERs between a healthy state and a damaged state with three missing SBM mounting screws. Acoustic discrete DF-ER is shown in (a) for the healthy system condition and (b) in the damaged state with main spectral changes indicated. (c) Acoustic noise DF-ER in the healthy state, and (d) in a damaged condition with main spectral changes. Significant amplitude differences in the SV-spectrum are evident in the acoustic responses. (e) AMB RD-M of the discrete DF-ER in the healthy and damaged states.

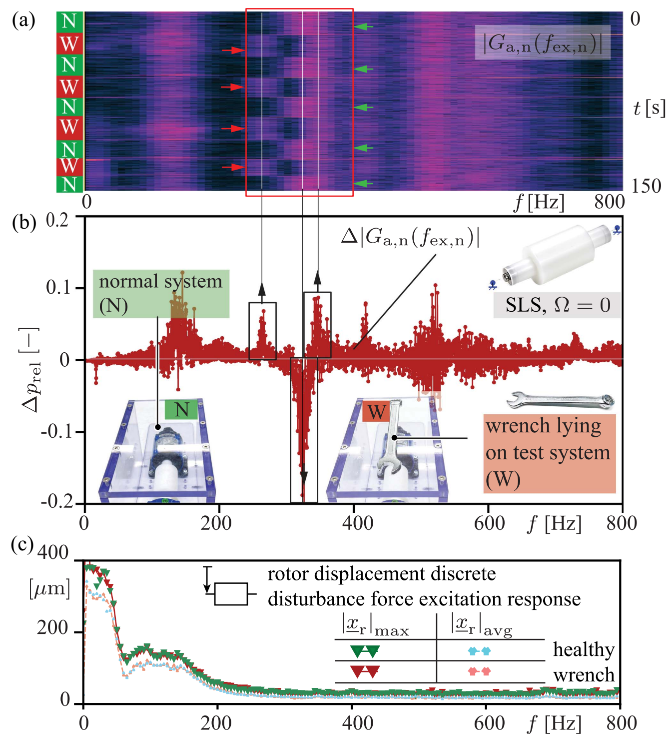


Fig. 9. (a) Spectrogram of noise DF-ER of repeated wrench placement on the test-system at SLS, with an indication of the normal system without wrench (N) and with wrench (W). (b) Difference of noise DF-ERs with and without wrench at SLS. (c) RD-M of discrete DF-ER with and without wrench.

noise DF-ER in SLS in healthy condition, and in Fig. 8(d) in damaged condition. Significant amplitude differences in the SV-spectra are evident for both acoustic predictions and are indicated. The corresponding acoustic responses for both methods for the same system condition match well, i.e., both are capable of predicting the system fault at SLS already. The lost stiffness due to the missing screws leads to increased vibration amplitude in the RD-M. However, changes in the SV-spectrum are not unveiled by RD-M. While a fault close to the RD-M location can be detected by RD-M, as the next case study shows, more remote faults cannot be detected by RD-M, but with the acoustic methods.

### C. Application Case Study 3: Forgotten Maintenance Tool

To show the higher sensitivity of the proposed acoustic methods compared with the AMB RD-M with increasing distance to the RD-M sensing location, a case is shown exemplary, where the acoustic noise-based method can detect the presence of a forgotten maintenance wrench lying on the test-system. The spectrogram in Fig. 9(a) shows the spectral difference when the wrench is placed (W) compared with when it is not (N). It was placed four times and removed four times, which is clearly visible in the presented spectrogram. Fig. 9(b) shows the difference in the noise DF-ER between these two cases. The SV-spectrum changes in Fig. 9(a) are identified in Fig. 9(b) in the form of nonsymmetric difference peaks, which differ from the symmetric peaks due to noisy signals. The noise DF-ER method is accordingly sensitive enough to detect a wrench placed on the test-system already in SLS. The AMB RD-M shows in Fig. 9(c) no signs of detection of the differences. In accordance with the presented theory in this article, it does not correlate with the SV-spectrum.

## VI. Conclusion

In this article, it was shown with theory and experimentally that RD-M fails to adequately measure mechanical resonances of AMB systems. Two novel acoustic DF-ER methods to predict the SV spectrum already in SLS were presented. They were further validated with 3D-FEM modal analysis and experimental ramp-up of the rotor speed. Three application case studies were presented: identification of mechanical resonance speed ranges already at SLS, detection of missing AMB mounting screws, and detection of a forgotten maintenance tool lying on the test-system housing. System failure risks can, therefore, be predicted safely before rotor speed is ramped-up. The fast measurement procedure, in the case of the natural noise response, even instantaneous feedback, allows for future live trial-and-error system optimization, e.g., adding dampers or stiffening elements, with quantifiable evaluation of the applied measures. The demonstrated capability for condition monitoring may be used in the future to capture acoustic "fingerprints" of industrial AMB systems, and their condition monitoring. Future applications may combine the presented methods with data-processing methods including machine learning.

## Acknowledgment

The authors would like to thank Levitronix GmbH for their scientific as well as technical contributions.

## References

[1] M. Hutterer and M. Schroedl, "Stabilization of active magnetic bearing systems in the case of defective sensors," *IEEE/ASME Trans. Mechatron.*, vol. 27, no. 5, pp. 3672–3682, Oct. 2022.

[2] A. H. Pesch and P. N. Scavelli, "Condition monitoring of active magnetic bearings on the Internet of Things," *Actuators*, vol. 8, no. 1, 2019, Art. no. 17.

[3] G. Schweitzer and E. H. Maslen, *Magnetic Bearings: Theory, Design, and Application to Rotating Machinery*. Berlin, Germany: Springer, 2009.

[4] R. Gouws, "Condition monitoring of active magnetic bearing systems," Ph.D. dissertation, Dept. Elect. Electron. Eng., North-West Univ., Potchefstroom, South Africa, 2007.

[5] M. K. Mueller, "On-line process monitoring in high speed milling with an active magnetic bearing spindle," Ph.D. dissertation, Inst. Robot., ETH Zürich, Zürich, Switzerland, 2002.

[6] M. N. Sahinkaya, M. O. T. Cole, and C. R. Burrows, "Fault detection and tolerance in synchronous vibration control of rotor-magnetic bearing systems," *Proc. Inst. Mech. Engineers, Part C: J. Mech. Eng. Sci.*, vol. 215, no. 12, pp. 1401–1416, 2001.

[7] R. R. Humphris, P. E. Allaire, D. W. Lewis, and L. E. Barrett, "Diagnostic and control features with magnetic bearings," in *Proc. 24th Intersociety Energy Convers. Eng. Conf.*, 1989, pp. 1491–1498.

[8] S. Kim and C. Lee, "Diagnosis of sensor faults in active magnetic bearing system equipped with built-in force transducers," *IEEE/ASME Trans. Mechatron.*, vol. 4, no. 2, pp. 180–186, Jun. 1999.
[9] N. Amati and E. Brusa, "Vibration condition monitoring of rotors on AMB fed by induction motors," in *Proc. IEEE/ASME Int. Conf. Adv. Intell. Mechatron.*, 2001, pp. 750–756.
[10] G. B. Gallego et al., "On-line micro-vibration measurement method for Lorentz-type magnetic-bearing space actuators," *Mechatronics*, vol. 64, 2019, Art. no. 102283.
[11] W. Wang and O. A. Jianu, "A smart sensing unit for vibration measurement and monitoring," *IEEE/ASME Trans. Mechatron.*, vol. 15, no. 1, pp. 70–78, Feb. 2010.
[12] G. Michau, G. Frusque, and O. Fink, "Fully learnable deep wavelet transform for unsupervised monitoring of high-frequency time series," in *Proc. Nat. Acad. Sci.*, vol. 119, no. 8, 2022, Art. no. e2106598119.
[13] X. Rui, J. Liu, Y. Li, L. Qi, and G. Li, "Research on fault diagnosis and state assessment of vacuum pump based on acoustic emission sensors," *Rev. Sci. Instrum.*, vol. 91, no. 2, 2020, Art. no. 025107.
[14] J. L. F. Chacon, "Fault detection in rotating machinery using acoustic emission," Ph.D. dissertation, Dept. Electron. Elect. Eng., Brunel Univ. London, London, U.K., 2015.
[15] J. N. Schoess, "Rotor acoustic monitoring system (RAMS) - A fatigue crack detection system," *Proc. SPIE*, vol. 2717, pp. 212–218, 1996.
[16] G. T. Venkatesan, D. West, K. M. Buckley, A. H. Tewfik, and M. Kaveh, "Automatic fault monitoring using acoustic emissions," in *Proc. IEEE Int. Conf. Acoust., Speech, Signal Process.*, 1997, pp. 1893–1896.
[17] L. Lin and F. Chu, "HHT-based AE characteristics of natural fatigue cracks in rotating shafts," *Mech. Syst. Signal Process.*, vol. 26, pp. 181–189, 2012.
[18] D. D. Quinn, G. Mani, M. E. F. Kasarda, T. Bash, D. J. Inman, and R. G. Kirk, "Damage detection of a rotating cracked shaft using an active magnetic bearing as a force actuator - analysis and experimental verification," *IEEE/ASME Trans. Mechatron.*, vol. 10, no. 6, pp. 640–647, Dec. 2005.
[19] C. H. Marais, "High speed flexible rotor active magnetic bearing control," Ph.D. dissertation, Sch. Elect., Electron. Comp. Eng., North-West Univ., Potchefstroom, South Africa, 2006.
[20] G. E. Piper, J. M. Watkins, and O. G. Thorp III, "Active control of axial-flow fan noise using magnetic bearings," *J. Vib. Control*, vol. 11, no. 9, pp. 1221–1232, 2005.
[21] G. B. Gallego, L. Rossini, T. Achtnich, D. M. Araujo, and Y. Perriard, "Novel generalized notch filter for harmonic vibration suppression in magnetic bearing systems," *IEEE Trans. Ind. Appl.*, vol. 57, no. 6, pp. 6977–6987, Nov./Dec. 2021.
[22] I. Inasaki, T. Blum, I. Suzuki, H. Itagaki, and M. Sato, "A practical mounting device for an acoustic emission sensor for the failure detection of multipoint cutting tools," *Trans. Inst. Syst., Control Inf. Engineers*, vol. 2, no. 6, pp. 210–221, 1989.
[23] P. K. Wong and J. S. Biao, "Fault diagnosis of induction motors under untrained loads with a feature adaptation and improved broad learning framework," *IEEE/ASME Trans. Mechatron.*, vol. 27, no. 5, pp. 3041–3052, Oct. 2022.
[24] O. Mey et al., "Condition monitoring of drive trains by data fusion of acoustic emission and vibration sensors," *Processes*, vol. 9, 2021, Art. no. 1108.
[25] ANSYS, "NVH solutions for electric vehicles," , Canonsburg, PA, USA, ANSYS Inc., White Paper, 2019.
[26] P. Kotter, "Vibroacoustics of electrical drive systems," Ph.D. dissertation, Inst. Mach. Tools Manuf. IWF, ETH Zürich, Zürich, Switzerland, 2019.
[27] P. Kotter, D. Morisco, M. Boesing, O. Zirn, and K. Wegener, "Noise-vibration-harshness-modeling and analysis of a permanent-magnetic disc rotor axial-flux electric motor," *IEEE Trans. Magn.*, vol. 54, no. 3, Mar. 2018, Art. no. 8101604.
[28] P. Kotter, W. Bischof, R. Kennel, O. Zirn, and K. Wegener, "Noise-vibration-harshness-modeling and analysis of induction drives in e-mobility applications," in *Proc. IEEE Int. Electric Mach. Drives Conf.*, 2017, pp. 1–8.
[29] M. Boesing and R. W. De Doncker, "Exploring a vibration synthesis process for the acoustic characterization of electric drives," *IEEE Trans. Ind. Appl.*, vol. 48, no. 1, pp. 70–78, Jan./Feb. 2012.
[30] A. Gilson, G. Verez, F. Dubas, D. Depernet, and C. Espanet, "Design of a high-speed permanent-magnet machine for electrically-assisted turbocharger applications with reduced noise emissions," in *Proc. IEEE Int. Electric Mach. Drives Conf.*, 2017, pp. 1–6.
[31] E. J. Hubmann, C. F. Blaser, S. Erismann, D. Steinert, T. Nussbaumer, and J. W. Kolar, "Magnetically self-bearing drive system for ultracentrifugation: Towards 100'000 rpm and 200'000 g," in *Proc. IEEE Int. Conf. Elect. Mach. Syst.*, 2021, pp. 88–94.
[32] G. Schweitzer, "Active magnetic bearings - Chances and limitations," in *Proc. 6th Int. Conf. Rotor Dyn.*, 2002, pp. 1–14.
[33] R. Larsonneur, "Principle of active magnetic suspension," in *Magnetic Bearings*, G. Schweitzer and E. H. Maslen, Eds. Berlin, Germany: Springer, 2002, pp. 27–68.
[34] "Product specifications Beta 58 A supercardioid dynamic vocal microphone," Shure Incorporated, Product Datasheet, 2015. [Online]. Available: www.shure.com
[35] J. Q. Sun, M. R. Jolly, and M. A. Norris, "Passive, adaptive and active tuned vibration absorbers - A survey," *Trans. ASME*, vol. 117(B), pp. 234–242, 1995.
[36] M. Hosek and N. Olgac, "A single-step automatic tuning algorithm for the delayed resonator vibration absorber," *IEEE/ASME Trans. Mechatron.*, vol. 7, no. 2, pp. 245–255, Jun. 2002.
[37] D. Pilbauer, T. Vyhlídal, and N. Olgac, "Delayed resonator with distributed delay in acceleration feedback - Design and experimental verification," *IEEE/ASME Trans. Mechatron.*, vol. 21, no. 4, pp. 2120–2131, Aug. 2016.
[38] *Mechanical Vibration - Vibration of Rotating Machinery Equipped With Active Magnetic Bearings - Part 4: Technical Guidelines*, Standard ISO 14839-4, 2012.
[39] R. Khatri, L. Hawkins, M. O. Neri, F. Cangioli, and D. Biliotti, "Design and prototype test data for a 300 kW AMB-supported turbine generator for natural gas pressure letdown," in *Proc. ASME Turbo Expo: Turbomachinery Tech. Conf. Expo.*, 2019, Art. no. V07BT34A030.
[40] E. H. Maslen, P. E. Allaire, M. D. Noh, and C. K. Sortore, "Magnetic bearing design for reduced power consumption," *ASME J. Tribology*, vol. 118, no. 4, pp. 839–846, 1996.
[41] M. O. T. Cole and W. Fakkaew, "An active magnetic bearing for thin-walled rotors: Vibrational dynamics and stabilizing control," *IEEE/ASME Trans. Mechatron.*, vol. 23, no. 6, pp. 2859–2869, Dec. 2018.
[42] J. R. Pierce, "Physical sources of noise," *Proc. IRE*, vol. 44, no. 5, pp. 601–608, May 1956.

**Emanuel J. Hubmann** (Graduate Student Member, IEEE) received the B.Sc. and M.Sc. degrees in mechanical engineering in 2016 and 2018, respectively, from the Swiss Federal Institute of Technology (ETH Zurich), Zurich, Switzerland, where he has been working toward the Ph.D. degree in advanced mechatronic systems and magnetic levitation with the Power Electronic Systems Laboratory (PES) since 2019.

He was active in organizations, such as J. Wagner AG, Swiss Armed Forces, Hitachi Zosen Inova AG, BRUSA Elektronik AG, Pediatric Heart Center Department of Surgery of the University Children's Hospital Zurich, and Levitronix GmbH. His research focuses on the field of mechatronics, especially in electric drive systems and magnetic levitation, for medical, biotech, and industrial applications.

Mr. Hubmann was the recipient of two Conference Prize Paper Awards and one Poster Award.

**Fabian Weissofner** was born in Kreuzlingen, Switzerland, in 1999. He received the B.Sc. degree in mechanical engineering in 2022 from ETH Zurich, Zurich, Switzerland, where he is currently working toward the master's degree in mechanical engineering.

He gained experience in his research area during his bachelor's thesis with the biofluiddynamics institution ARTORG Center for Biomedical Engineering Research, Bern, Switzerland, in 2021. In addition, he was with Biplast AG and is currently with with Levitronix GmbH. His research focuses on the specialization in biomedical applications.

**Daniel Steinert** was born in Roth, Germany, in 1987. He received the M.Sc. degree in mechatronics from the Dresden University of Technology, Dresden, Germany, in 2012, and the Ph.D. degree in bearingless motors from the Power Electronic Systems Laboratory of the Swiss Federal Institute of Technology Zurich (ETH Zurich), Zurich, Switzerland, in 2015, where he worked on high-speed bearingless motors.

He is currently with Levitronix GmbH, as the Head of the research group. His research interests include micromechatronics and precision engineering, bearingless motor topologies, control concepts, losses, and applications of bearingless motors.

**Thomas Nussbaumer** was born in Vienna, Austria, in 1975. He received the M.Sc. (Hons.) degree in electrical engineering from the Vienna University of Technology, Vienna, Austria, in 2001, and the Ph.D. degree in power electronics from the Swiss Federal Institute of Technology Zurich (ETH Zurich), Zurich, Switzerland, in 2004.

From 2001 to 2006, he was with the Power Electronic Systems Laboratory, ETH Zurich, where he was involved in research on modeling, design, and control of three-phase rectifiers, power factor correction techniques, and electromagnetic compatibility. Since 2006, he has been with Levitronix GmbH, Zurich, where he is currently the Vice President of R&D in research on bearingless motors, magnetic levitation, and permanent-magnet motor drives for the semiconductor and biotechnology industry. His research focuses on compact and high-performance mechatronic systems, including novel power electronics topologies, control techniques, drive systems, sensor technologies, electromagnetic interference, and thermal aspects.

**Johann W. Kolar** (Fellow, IEEE) received the M.Sc. degree in industrial electronics and control engineering and the Ph.D. degree in electrical engineering (*summa cum laude*) from the Vienna University of Technology, Vienna, Austria in 1997 and 1999 respectively.

He is currently a Full Professor and the Head of the Power Electronic Systems Laboratory with the Swiss Federal Institute of Technology (ETH Zurich), Zurich, Switzerland. He has authored or coauthored more than 900 journal and conference papers, and four book chapters, and has filed more than 200 patents. His research interests include ultra-compact/efficient WBG converter systems, ANN-based design procedures, solid-state transformers, ultra-high speed drives, and bearingless motors.

Dr. Kolar has proposed numerous novel converter concepts including the Vienna rectifier, the sparse matrix converter, and the Swiss rectifier. He has spearheaded the development of x-million rpm motors, and has pioneered fully automated multiobjective power electronics design procedures. He has graduated more than 80 Ph.D. students. He has presented more than 30 educational seminars at leading international conferences. from 2012–2016, he was an IEEE PELS Distinguished Lecturer. He was the recipient of more than 40 IEEE Transactions and Conference Prize Paper Awards, the 2014 IEEE Power Electronics Society R. David Middlebrook Achievement Award, the 2016 IEEE PEMC Council Award, the 2016 IEEE William E. Newell Power Electronics Award, the 2021 EPE Outstanding Achievement Award, and two ETH Zurich Golden Owl Awards for excellence in teaching. He was elected to the U.S. National Academy of Engineering as an International Member in 2021.